Simulations of femtosecond atmospheric filaments enhanced by dual pulse molecular alignment

J. P. Palastro, T. M. Antonsen Jr., S. Varma, Y.-H. Chen, and H. M. Milchberg
Institute for Research in Electronics and Applied Physics, University of Maryland, College Park, Maryland 20740, USA
(Received 17 March 2012; published 27 April 2012)

A laser pulse propagating through the atmosphere self-focuses due to the nonlinear index of refraction modifications from the instantaneous electronic and delayed rotational responses of the air molecules. If the pulse power is sufficient, the focused pulse intensity can surpass the ionization threshold, resulting in a plasma filament. The balance between defocusing due to plasma refraction and focusing due to the instantaneous and delayed responses results in extended propagation at high intensities. Because the rotational response induced by the first pulse (the pump pulse) is periodic in time, owing to quantum-mechanical discreteness of the rotational eigenfrequencies of the molecules, a subsequent laser pulse (the probe pulse), delayed at the recurrence period, experiences a propagating wake of index modification left behind by the previous pulse. Here, we present propagation simulations based on a recent experiment [Varma *et al*. (unpublished)] showing that axial extension of the plasma filament and probe pulse shaping imposed by the molecular alignment wake are sensitive to probe delay changes of as little as 10 fs.

DOI: 10.1103/PhysRevA.85.043843 PACS number(s): 42.65.Re, 52.38.Hb, 52.50.Jm, 92.60.Ta

I. INTRODUCTION

Ultrashort laser pulses propagating in atmosphere self-focus by modifying the local dielectric susceptibility through interactions with N_2 and O_2 [1,2]. During focusing, as the laser pulse intensity increases, the electron clouds of the N_2 and O_2 molecules become increasingly deformed, and the axes of the molecules become partially aligned with the laser polarization axis. These processes provide an intensity-dependent index of refraction with a radial profile mirroring that of the laser pulse. The nonlinear index acts as a traveling lens and imparts a radial phase shift that combats diffraction, helping to collimate the pulse. If the focusing is strong enough, the pulse can reach the breakdown intensity for air, creating a plasma filament. The plasma then refracts the pulse, lowering the intensity, and ionization terminates. Under certain circumstances, the process of self-focusing, ionization, and refraction can occur more than once before the pulse finally diffracts away leading to spatially extended filaments [3].

For linear diatomic molecules as found in air, the dielectric susceptibility is composed of two contributions: the instantaneous electronic response and the delayed rotational response. The instantaneous electronic response arises from the induced dipole moment acquired by atoms in the presence of the laser field. At atmospheric temperatures, the electrons within the molecules are present in the ground state with response times much shorter than the optical period. As a result, the presence of the laser electric field causes a time-dependent separation between the electron cloud center and the nucleus that oscillates at the laser frequency. The laser pulse then interacts with the induced dipole moment setting up a polarization current that feeds back onto the laser through an intensity-dependent index of refraction.

The delayed rotational response occurs due to the aligning of N_2 or O_2 molecules along the laser polarization axis. For typical diatomic molecules, the polarizability is anisotropic being larger along the molecular axis than perpendicular to it. In general, the molecular axes will be randomly oriented in atmosphere. Because of the random orientation, the initial ensemble average polarizability of the gas is isotropic. As the laser pulse turns on, the dipoles experience a torque that tends to bring them into alignment with the laser electric field. Because the alignment must overcome the inertia of the nuclei, the process occurs on a longer time scale than the instantaneous response. The delayed nature of the alignment provides a susceptibility that is nonlocal in time: The alignment at any time within the pulse depends on the intensity at previous times. A consequence of this for short pulses is that the susceptibility depends not only on the intensity through the instantaneous response, but also on the energy fluence of the pulse.

After the initial alignment of diatomic molecules, the response decays but reforms itself periodically [4–9]. Revivals in the molecular alignment result from the fact that the rotational quantum eigenfrequencies are integer related [$E = \hbar\Omega_0 j(j+1)$, where j is the total angular momentum quantum number and Ω_0 is the ground-state rotation rate]. In addition, the phase of the recurrence propagates at the group velocity of the original pulse. Thus, a second properly timed pulse not only will experience the nonlinear susceptibility it generates, but also will experience the delayed rotational response of the preceding pulse. Examining the self-consistent propagation of a second pulse co-propagating with the recurrence in the rotational susceptibility is the focus of this paper.

The potential for extended propagation at high intensities has led to several investigations into nonlinear atmospheric propagation of single pulses both experimental and theoretical [10–17]. Several multiple pulse studies have also been conducted [18–24]. Bartels *et al*. have conducted experiments demonstrating the phase modulation and spectral broadening of probe pulses in the susceptibility recurrence of CO_2 [18]. Fibich *et al*. have performed simulations of counterpropagating lasers in a generic medium with the instantaneous susceptibility but without the delayed molecular response [19]. An experiment exploring the effects on high-intensity pulse propagation of molecular alignment recurrences was that of Varma *et al*. [21]. They showed that, if an intense probe pulse was injected at various delays into a pump-filament-induced molecular alignment wake in air, the probe filament could

be laterally displaced and trapped, enhanced, or destroyed depending on the pump-probe delay. A more recent experiment has explored the pump-probe effects on filament electron-density and probe pulse shaping [23].

Calegari *et al*. have performed experiments and simulations of strong pump-weak probe propagation with the probes delayed with respect to the rotational recurrence period [24]. Their paper considers only the linear propagation of the probe in a single gas species. This is in contrast to the work presented here, which considers the nonlinear evolution of high-power probe pulses delayed near the recurrence period in both N_2 and O_2. The inclusion of two gas species is necessary for atmospheric propagation simulations. While the instantaneous and delayed susceptibilities are dominated by N_2 due to the large fractional composition, the ionization is dominated by O_2, which requires lower intensities in the multiphoton regime [25,26]. Recently, Wahlstrand *et al*. have used spectral interferometry to provide the most direct and precise measurements of the instantaneous nonlinear index and the molecular linear polarizability asymmetry [27], which we use to calibrate our simulations. With the simulations, we consider the extension of plasma filaments for both identical and cross polarization for several delays. We also examine the structure and evolution of the probe pulse due to the recurrence susceptibility generated by the pump and the self-consistent index modifications generated by the probe itself.

This paper is organized as follows. In Sec. II, we describe the propagation model and the derivation of the wave equation in terms of the vector potential used in our simulations. Section III includes a description of the response models used in the simulation, including models for the instantaneous electronic response, the delayed rotational response, ionization, ionization damping, and the plasma response. Section IV contains our simulation results for a single pump pulse and a probe pulse at varying delays with respect to the pump pulse for the situations of cross and identical polarizations. Finally, in Sec. V, we conclude with the summary and conclusions of our paper.

II. PROPAGATION MODEL

We begin by writing the nonlinear wave equation for the vector potential as follows:

$$\nabla\times\nabla\times\vec{A}+\frac{1}{c^2}\frac{\partial^2\vec{A}}{\partial t^2}=\frac{4\pi}{c}\frac{\partial\vec{P}}{\partial t}, \tag{1}$$

where $\vec{P}=\vec{P}(\vec{x},t:\vec{A})$ is the polarization vector, which can be a nonlinear function of the electric field and by extension $\vec{A}$. Standard vacuum propagation is accounted for by the wave operator on the left-hand side (LHS) of Eq. (1), and modifications to the vacuum index of refraction due to the dielectric response of N_2 and O_2 are grouped into the polarization vector on the right-hand side (RHS). In particular, the polarization vector will include the effects of plasma density via ionization, the instantaneous electronic response, the delayed rotational response, and linear dispersion. Here, we will consider the evolution of the laser pulse for frequencies near the initial central frequency ω_0, thus, nonlinear processes associated with harmonic generation will be ignored. Furthermore, we will consider circularly symmetric propagation such that the vector potential and polarization vector have transverse variation in radius only.

Because the plasma density in a typical filament is small, we apply the condition $\nabla\cdot\vec{A}=0$ to Eq. (1). We note that this is not a gauge choice but an approximation. In particular, we require $\omega_p^2/\omega_0^2\ll 1$, where $\omega_p^2=4\pi e^2\rho_e/m_e$, ρ_e is the electron density, e is the fundamental unit of charge, m_e is the electron mass, and c is the speed of light. The condition $\nabla\cdot\vec{A}=0$ also provides a relation between $A_\perp$ and A_z : A_z can be found without solving an additional wave equation. From here on, we only consider the transverse vector potential, and the subscript $\perp$ is understood.

To include linear dispersion, we write $P=P_L+P_{NL}$, where P_L represents the linear in electric-field contribution to the polarization and P_{NL} is the nonlinear contribution. For a linear medium, the polarization and electric field can be related via the constitutive relation $\bar{P}_L(\omega)=\chi(\omega)\bar{E}(\omega)$, where χ is the susceptibility, E is the electric field, and the overbars denote temporal Fourier transforms. Using $\bar{E}=i(\omega/c)\bar{A}$ and $\varepsilon(\omega)=1+4\pi\chi(\omega)$, the vector potential can be related to the polarization through the dielectric function $\varepsilon(\omega)$ by $\bar{P}_L(\omega)=i\omega[\varepsilon(\omega)-1]\bar{A}(\omega)/4\pi c$. The temporal Fourier transform of Eq. (1) is then

$$\left[\nabla^2+\varepsilon(\omega)\frac{\omega^2}{c^2}\right]\bar{A}=i\omega\frac{4\pi}{c}\bar{P}_{NL}. \tag{2}$$

To avoid a convolution integral in the time domain due to the product $\varepsilon(\omega)\bar{A}$, we Taylor expand the dielectric function around the laser central frequency ω_0 as follows:

$$\frac{\omega^2}{c^2}\varepsilon(\omega)=\gamma_0-\gamma_1\delta\omega+\gamma_2(\delta\omega)^2, \tag{3}$$

where $\delta\omega=\omega_0-\omega$ is the frequency shift away from the laser central frequency, $\gamma_0=c^{-2}\omega_0^2\varepsilon(\omega_0)$, $\gamma_1=c^{-2}[\partial_\omega(\omega^2\varepsilon)]|_{\omega=\omega_0}$, and $\gamma_2=\frac{1}{2}c^{-2}[\partial_\omega^2(\omega^2\varepsilon)]|_{\omega=\omega_0}$. For atmospheric conditions, the expansion is valid as the dielectric function is a weak function of frequency near optical frequencies [28]. Upon inverse Fourier transforming with respect to the variable $\delta\omega$, we find

$$\left[\nabla^2+\gamma_0+i\gamma_1\frac{\partial}{\partial t}-\gamma_2\frac{\partial^2}{\partial t^2}\right]\hat{A}=-\frac{4\pi}{c}\left[i\omega_0-\frac{\partial}{\partial t}\right]\hat{P}_{NL}, \tag{4}$$

where $\hat{A}(\vec{x},t)=\frac{1}{2\pi}\int\bar{A}(\vec{x},\omega_0+\delta\omega)e^{i\delta\omega t}d(\delta\omega)$ and $\hat{P}_{NL}(\vec{x},t)=\frac{1}{2\pi}\int\bar{P}_{NL}(\vec{x},\omega_0+\delta\omega)e^{-i\delta\omega t}d(\delta\omega)$. Equation (5) determines the evolution of the laser pulse enveloped about its central frequency. In addition, we consider the envelope of the laser pulse around the wave number k, which is determined shortly hereafter. Inserting $\hat{A}(\vec{x},t)=e^{ikz}A(\vec{x},t)$ and $\hat{P}_{NL}(\vec{x},t)=e^{ikz}P_{NL}(\vec{x},t)$ into Eq. (4), provides

$$\left[\nabla_\perp^2+(\gamma_0-k^2)+i\gamma_1\frac{\partial}{\partial t}-\gamma_2\frac{\partial^2}{\partial t^2}+2ik\frac{\partial}{\partial z}+\frac{\partial^2}{\partial z^2}\right]A=-\frac{4\pi}{c}\left[i\omega_0-\frac{\partial}{\partial t}\right]P_{NL}. \tag{5}$$

For short laser pulses, it is useful to introduce a moving frame with speed c_f that can be chosen for convenience. The associated coordinates are $\xi=c_f t-z$, representing

distance back from the head of the laser pulse, and $z = z$, representing distance along the propagation path. Under the variable transformation, Eq. (5) becomes

$$\left[\nabla_\perp^2 + \frac{\partial^2}{\partial z^2} + 2\frac{\partial}{\partial z}\left(ik - \frac{\partial}{\partial \xi}\right) + k^2\beta_0 + ik\beta_1\frac{\partial}{\partial \xi} - \beta_2\frac{\partial^2}{\partial \xi^2}\right]A = -\frac{4\pi}{c}\left[i\omega_0 - \frac{c_f}{c}\frac{\partial}{\partial \xi}\right]P_{NL}, \quad (6)$$

where $\beta_0 = k^{-2}\gamma_0 - 1$, $\beta_1 = k^{-1}\gamma_1 c_f - 2$, and $\beta_2 = \gamma_2 c_f^2 - 1$. It is now useful to express the linear dielectric constant as $\varepsilon(\omega_0) = 1 + \delta\varepsilon(\omega_0)$, where $\delta\varepsilon(\omega_0)$ is the change in the linear dielectric function due to the presence of atmosphere. As we see, the typical index modifications associated with atmospheric propagation are small. One can then show that, if $c_f = c_g = (\partial\omega/\partial k)|_{\omega=\omega_0}$ and $k = k_0(1 + \frac{1}{2}\delta\varepsilon)$, where $k_0 = \omega_0/c$, then $k\beta_1 = 0$ and $k^2\beta_0 = 0$ for order $(\delta\varepsilon)^2$. The third term in Eq. (6), within the parentheses, is responsible for local wave-number shifts within the pulse $\partial_\xi \sim -i\ \delta k$, and the second-order term in z is associated with modifications to the Doppler-shifted frequency $\partial_z \sim i(\delta\omega - c\ \delta k)$ in the moving frame. Because the atmosphere is optically thin $\delta\omega \simeq c\ \delta k$, the second-order derivative in z can be ignored along with $\delta\varepsilon\ \partial_z$. Finally, if the phase evolution of the polarization within the laser pulse is much slower than the laser pulse central frequency, we can drop the second term on the RHS of Eq. (6). In the Appendix, we consider the effect of this term on the energy conservation of the laser pulse. Applying these approximations, we end up with the following equation describing the evolution of the laser pulse enveloped around the frequency ω_0 and wave number $k = k_0(1 + \frac{1}{2}\delta\varepsilon)$:

$$\left[\nabla_\perp^2 + 2\frac{\partial}{\partial z}\left(ik_0 - \frac{\partial}{\partial \xi}\right) - \beta_2\frac{\partial^2}{\partial \xi^2}\right]A = -i\frac{4\pi\omega_0}{c}P_{NL}. \quad (7)$$

The coefficient $\beta_2 = \omega_0 c(\partial^2 k/\partial\omega^2)|_{\omega=\omega_0}$ accounts for group-velocity dispersion: Different frequencies travel at different group velocities resulting in spreading of the laser pulse as it propagates.

III. ATMOSPHERIC RESPONSE MODEL

We now consider the physical processes contributing to the nonlinear polarization. In general, the polarization can be expressed as $P_{NL} = -\chi_{NL}(ik_0 - \partial_\xi)A$, where χ_{NL} is the nonlinear susceptibility of the atmosphere. In the Appendix, we show that the ξ derivative has a minimal effect on the energy and phase evolution of the pulse, and thus, from here on, we use $P_{NL} = -ik_0\chi_{NL}A$. The susceptibility can be written as a sum of three contributions as follows:

$$\chi_{NL} = \chi_{\text{elec}} + \chi_{\text{rot}} + \chi_{\text{free}}, \quad (8)$$

where χ_{elec} is the instantaneous electronic response, χ_{rot} is the molecular rotational response, and χ_{free} is the free-electron response. Each of these will be considered below. For now, we note that the index of refraction is related to the susceptibility by $n \simeq 1 + 2\pi\chi$ and that both electronic and rotational responses contribute a positive χ leading to focusing, whereas, the plasma contributes a negative χ leading to refraction.

A. Electronic and rotational responses

In the presence of an external electric field, the electron cloud of an atom or molecule becomes distorted resulting in an induced dipole moment. At atmospheric temperatures, N_2 and O_2 exist primarily in their electronic ground states. Thus, for wavelengths much larger than the resonant excitation frequencies, the electron cloud can adjust instantaneously to the field of the laser pulse. For N_2 and O_2, significant electronic excitation and absorption occur at wavelengths of $\lambda \sim 120$ and 175 nm, respectively. To motivate the electronic and rotational responses, we consider the classical picture, which has had qualitative success modeling the evolution of the molecular dipole moment. The shortcoming of the classical picture is that linear and nonlinear polarizability coefficients appear as parameters, which need to be found via experiments or from a full Schrödinger-equation treatment of the molecule. We note that quantizing the classical rotational Hamiltonian has predicted revivals in the rotational response but still requires specification of polarizabilities.

The simplest picture describing the response of a linear diatomic molecule to an external field is the rigid-rotor model: two positive nuclei of fixed separation with associated electron orbitals. The polarizability is determined by an ensemble average of molecular dipole moments $\vec{p} = -e\vec{x}$ through the expression $\vec{P} = \rho\langle\vec{p}\rangle$, where $\vec{x}$ measures the separation between the centers of the electronic and nuclear charges for each molecule, ρ is the number density, and $\langle X\rangle$ represents an ensemble average of the quantity X. The electron clouds are bound to the nuclei by an anharmonic potential. At lowest order in the electric field, the electron oscillates at the laser frequency with an amplitude along each molecular axis proportional to the linear polarizability associated with that axis. In particular, $\vec{p}_L = \alpha_\perp\vec{E} + \Delta\alpha\ \hat{s}_\parallel(\hat{s}_\parallel \cdot \vec{E})$, where $\Delta\alpha = \alpha_\parallel - \alpha_\perp$, $\alpha_\parallel$, and $\alpha_\perp$ are the linear polarizabilities along and perpendicular, respectively, to the molecular bond axis, and $\hat{s}_\parallel$ is a unit vector along the axis of the molecule. The polarizability can be decomposed into a portion that is parallel to the laser electric field and a portion perpendicular: $\vec{p}_L = \vec{p}_{L,\parallel} + \vec{p}_{L,\perp}$, where $\vec{p}_{L,\parallel} = (\alpha_\perp + \Delta\alpha\ \cos^2\theta)\vec{E}$ and θ is the angle between the polarization direction and the molecular bond axis. On averaging over an ensemble of molecules, the contributions of $\vec{p}_{L,\perp}$ cancel. If we further assume no net molecular orientation relative to $\vec{E}$ and average over θ, we find $\langle\vec{p}_{L,\parallel}\rangle = (\alpha_\perp + \frac{1}{3}\Delta\alpha)\vec{E}$. This contribution is included in the dispersion for air.

As the electron clouds oscillate in the electric field, they experience the anharmonicity of the potential providing a correction to their oscillation amplitude. This correction provides the nonlinear instantaneous electronic response (as well as third harmonic generation, which is not considered here). In particular, we can write the lowest-order nonlinear instantaneous dipole moment as $p_k = \beta_{ijk}E_iE_jE_k$ where the sum over repeated indices is implied and the β_{ijk} parametrize the anharmonicity of the potential. In the absence of polarization rotation, this simplifies to $p_k = \beta_{iik}|E_i|^2E_k$ or simply $p_k = \beta_{ik}|E_i|^2E_k$. For diatomic molecules composed of identical atoms, β_{ik} is a symmetric matrix providing only three matrix elements. We can then define the three nonlinear polarizabilities as $\beta_\parallel$, $\beta_\perp$, and $\beta_\times$, which represent the

polarizability along the molecular axis, perpendicular to the molecular axis, and the cross polarizability. Thus, the nonlinear electronic dipole moment can be expressed as $\vec{p}_{\rm elec} = \alpha_\perp^{(3)}\vec{E} + \Delta\alpha^{(3)}(\hat{s}_\parallel \cdot \vec{E})\hat{s}_\parallel$, where $\alpha_\perp^{(3)}(\vec{E}) = \beta_\perp|\vec{E}|^2 - \Delta\beta_\perp(\hat{s}_\parallel \cdot \vec{E})^2$, $\Delta\alpha^{(3)}(\vec{E}) = (\Delta\beta_\parallel + \Delta\beta_\perp)(\hat{s}_\parallel \cdot \vec{E})^2 - \Delta\beta_\perp|\vec{E}|^2$, and $\Delta\beta_a = \beta_a - \beta_\times$. As above, the component of the dipole along the laser polarization axis is given by $\vec{p}_{\rm elec,\parallel} = (\alpha_\perp^{(3)} + \Delta\alpha^{(3)}\cos^2\theta)\vec{E}$, however, now the coefficients $\alpha_\perp^{(3)}$ and $\Delta\alpha^{(3)}$ are functions of the angle θ. Again, we assume no net molecular orientation relative to $\vec{E}$ and average over θ, yielding the electronic susceptibility,

$$\chi_{\rm elec} = \rho\tfrac{1}{5}\left(\beta_\parallel + \tfrac{8}{3}\beta_\perp + \tfrac{1}{3}\beta_\times\right)|k_0\vec{A}|^2, \tag{9}$$

where ρ is the number density. The coefficient in Eq. (9) can be related to the nonlinear instantaneous index of refraction as

$$n_2 = \frac{16\pi^2}{5}\frac{\rho}{c^2}\left(\beta_\parallel + \frac{8}{3}\beta_\perp + \frac{1}{3}\beta_\times\right). \tag{10}$$

Equation (10) expresses the macroscopic index of refraction in terms of the microscopic details of the bound-electron motion. In terms of macroscopic quantities, the total instantaneous susceptibility for atmosphere can be expressed as

$$\chi_{\rm elec} = \frac{1}{2\pi\rho_{\rm atm}}(\rho_{\rm N}n_{2,\rm N} + \rho_{\rm O}n_{2,\rm O})I_0|a|^2, \tag{11}$$

where $n_{2,j}$ is the nonlinear instantaneous index of refraction for each gas species at one atmosphere (we use N and O, but they are understood to represent the diatomic molecules), ρ_j is the atmospheric number density of each gas species, $\rho_{\rm atm}$ is the total atmospheric number density, $a = eA/m_ec^2$ is the normalized vector potential, and $I_0 = 8.6\times10^{18}$ W/cm^2 is the intensity for a laser pulse with a wavelength of 800 nm and $a = 1$. For the simulations presented here, we use the values $\rho_{\rm N}/\rho_{\rm atm} = 0.8$, $\rho_{\rm O}/\rho_{\rm atm} = 0.2$, $n_{2,\rm N} = 7.4\times10^{-20}$ cm^2/W, and $n_{2,\rm O} = 9.5\times10^{-20}$ cm^2/W [27].

The molecular rotational response arises from the anisotropy in the linear polarization with respect to the molecular axes that was discussed with regard to the linear response above. In a linear diatomic molecule, the electrons are less confined in the direction parallel to the bond axis than in the transverse direction: $\alpha_\parallel > \alpha_\perp$. Thus, an external electric field exerts a torque on a molecule if its axis is not aligned with the electric field. The torque results from the electron cloud dragging the nuclei such that the molecular bond axis is aligned with the polarization axis. Because the process involves motion of the nuclei, it occurs on a time scale much longer than the electron response. Recall from before that a linear dipole moment of an ensemble of molecules can be written as $\langle\vec{p}_{L,\parallel}\rangle = (\alpha_\perp + \Delta\alpha\langle\cos^2\theta\rangle)\vec{E}$ where, in the absence of net molecular alignment, $\langle\cos^2\theta\rangle = 1/3$. In the presence of the laser pulse, $\langle\cos^2\theta\rangle$ is a function of time representing the gradual alignment of the molecules along the polarization axis. We separate the contributions to the linear polarizability as $\langle\vec{p}_{L,\parallel}\rangle = (\alpha_\perp + \Delta\alpha/3)\vec{E} + \langle\vec{p}_{\rm rot}\rangle$. Recall that the first term is included in the linear susceptibility and gives rise to the quantity $\delta\varepsilon$. Accounting for both N_2 and O_2, the rotational susceptibility is then

$$\chi_{\rm rot}^s = \rho_{\rm N}\Delta\alpha_{\rm N}\left[\langle\cos^2\theta\rangle_{\rm N} - \tfrac{1}{3}\right] + \rho_{\rm O}\Delta\alpha_{\rm O}\left[\langle\cos^2\theta\rangle_{\rm O} - \tfrac{1}{3}\right], \tag{12}$$

where s denotes the susceptibility generated by the pulse itself and the difference in polarizabilities are $\Delta\alpha_{\rm N} = 7\times10^{-25}$ cm^3 and $\Delta\alpha_{\rm O} = 1.1\times10^{-24}$ cm^3 [27]. The alignment of the molecules is a nonlocal response of the medium depending on the time history of the laser pulse. As a result, $\langle\cos^2\theta\rangle$ for each species is expressed as a convolution in time of the form

$$\langle\cos^2\theta\rangle_i = \int_{-\infty}^{\xi} G_i(\xi - \xi')|\vec{E}(\xi')|^2 d\xi', \tag{13}$$

where $G_i(\xi)$ represents the Green's function for alignment when the laser pulse approximates an impulse. We note that Eq. (13) represents only the lowest order in the electric-field contribution to the rotational alignment $\langle\vec{p}_{\rm rot}\rangle \propto E_0^3$, where E_0 is the laser electric-field amplitude.

There are several models for $G_i(\xi)$, each with a varying degree of insight and approximation. In general, the models with the least approximation are those with the largest computational requirements. Here, we present a reduced model for $G_i(\xi)$ used in prior atmospheric propagation simulations but also expand this model to capture the quantum-mechanical (QM) phenomenon of rotational recurrences. We start by reviewing the standard alignment model. Using a classical theory for an ensemble of diatomic molecules that treats the molecules as classical rotors, the Green's function for the initial delayed response for a single species can be expressed as

$$G(\hat{\xi}) = \frac{\Delta\alpha}{15k_TM}\left[\hat{\xi} + \frac{1}{2}\pi^{1/2}(1 - 2\hat{\xi}^2)e^{-\hat{\xi}^2}\,{\rm erfi}(\hat{\xi})\right], \tag{14}$$

where $\hat{\xi} = k_T\xi$, $k_T = c^{-1}(2T/M)^{1/2}$, M is the molecular moment of inertia, T is the temperature in units of energy, and erfi is the imaginary error function [5]. However, performing a convolution integral with this function at every point in space requires a large number of computations $\sim N_\xi^2$, where N_ξ is the number of grid points in ξ, greatly extending simulation times. As an alternative, the response function G is modeled as a damped harmonic oscillator with the natural frequency, damping, and steady-state index chosen to fit Eq. (14) or QM density-matrix calculations. Thus, to determine the total susceptibility, a driven harmonic oscillator equation can be solved requiring only $\sim N_\xi$ computations. In particular, the rotational susceptibility for each gas is modeled using the equation,

$$\left[\frac{d^2}{d\xi^2} + 2\gamma_i\frac{d}{d\xi} + \omega_i^2\right]\chi_{{\rm rot},i}^s = \frac{1}{2\pi}\omega_i^2\bar{n}_{2,i}I_0|a(\xi)|^2. \tag{15}$$

Because we are interested in laser pulses with full width at half maxima (FWHM) less than 100 fs, the parameters ω_i, γ_i, and $\bar{n}_{2,i}$ are chosen to best match the initial rise up to the peak in the rotational response. For nitrogen, we find good agreement of the initial response for $\omega_{\rm N} = 0.0162$ rad/fs, $\gamma_{\rm N} = 0.0096$ fs^{-1}, and $\bar{n}_{2,\rm N} = 1.35\times10^{-19}$ cm^2/W, whereas, for oxygen, $\omega_{\rm O} = 0.0142$ rad/fs, $\gamma_{\rm N} = 0.006$ fs^{-1}, and $\bar{n}_{2,\rm O} = 3.2\times10^{-19}$ cm^2/W. A comparison of the results of Eq. (15) and the classical and QM models are shown in Fig. 1(a) for an impulse starting at 20 fs.

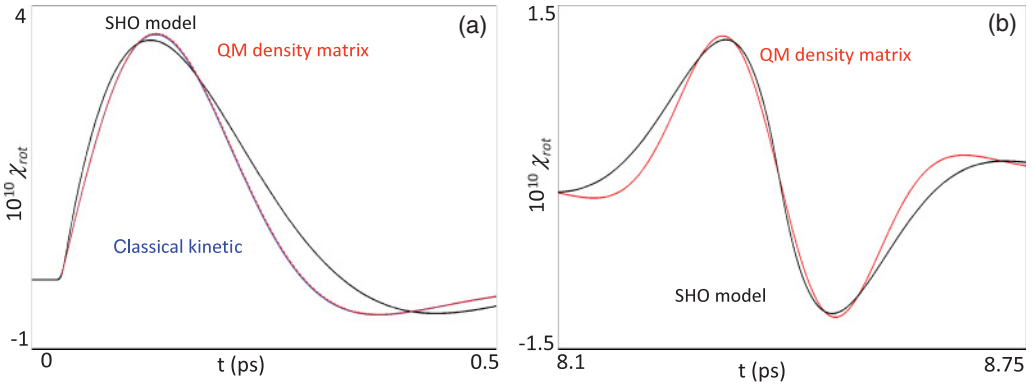

FIG. 1. (Color online) (a) Comparison of rotational susceptibilities from the SHO model in Eq. (15), the classical kinetic model, and the QM density-matrix theory for a pulse approximating an impulse starting at $t = 20$ fs with an intensity of $I = 1 \times 10^{10}$ W/cm^2 and a fluence of 5×10^{-5} J/cm^2. (b) Comparison of the rotational susceptibility after one full recurrence period in nitrogen modeled by Eq. (17) and the QM density-matrix theory result for a pulse approximating an impulse with an intensity of $I = 1 \times 10^{10}$ W/cm^2 and a fluence of 5×10^{-5} J/cm^2. Here, the probe pulse has its polarization rotated 90° from the pump pulse. In both figures, the SHO model is distinguished by the slower decay.

The delayed response model presented above eventually phase mixes away after a few hundred femtoseconds, leaving behind no modification to the susceptibility. Full QM density-matrix calculations have predicted and experiments have observed recurrences in the rotational response of the molecules due to the discrete eigenfrequencies of the molecules: $\omega_j = \hbar j(j+1)/2M$, where j is the total angular momentum eigenvalue [4,6,7]. Thus, a second laser pulse delayed from the initial pulse by the recurrence period will experience not only its own rotational index modification, but also an index modification generated by previous pulses. The linear perturbation density-matrix result for the Green's function is

$$G(\xi) = \frac{2}{15}\Delta\alpha \sum_{j=2}^{\infty} \frac{j(j-1)}{2j-1}(F_j - F_{j-2}) \sin\left[\frac{\hbar}{Mc}(2j-1)\xi\right], \tag{16}$$

where $F_j = Z^{-1} D_j \exp[-\frac{\hbar^2}{2MT} j(j+1)]$ is the field-free probability of a molecule in the ensemble being in state (j,m), here, m is the angular momentum value quantized along the laser polarization direction, $Z = \sum_{j=0} D_j(2j+1)\exp[-\frac{\hbar^2}{2MT} j(j+1)]$ is the partition function, and D_j is the degeneracy factor for different nuclear spin states having the same rotational eigenvalue [6]. The important aspect of Eq. (16) is that it is periodic with period $\tau = 2\pi M/\hbar$: for nitrogen and oxygen at $\tau = 8.375$ and $\tau = 11.57$ ps, respectively. We note that there are also half and quarter revivals at $\tau = \pi M/\hbar$ and $\tau = \pi M/2\hbar$, but here, we are interested in the evolution of a second pulse placed near the full recurrence time of nitrogen.

A convenient feature of Eq. (16) is that, when inserted into the convolution integral in Eq. (13), the sine functions in the summation are multiplicatively separable limiting the number of operations to $\sim N_\xi N_j$, where N_j is the number of terms in the summation. However, at standard atmospheric temperatures, $j = 10$ is the most populated state of N_2. Thus, a reasonable representation of the Green's function would require keeping about 30 terms in Eq. (16). Furthermore, each term would have to be followed for 8.4 ps, near 2 orders of magnitude longer than the pulse lengths.

Instead, we propose a delayed version of Eq. (15). Figure 1(b) shows a fundamental recurrence in the susceptibility of atmospheric N_2 at $T = 294$ K for the case of a δ-function pulse at $t = 20$ fs with fluence $\int I(t)dt = 5 \times 10^{-5}$ J/cm^2 as calculated by the QM density-matrix method. Plotted is the susceptibility that a probe pulse, with an electric field rotated 90° with respect to the pump, would experience. The recurrence time is $\tau = 8.375$ ps, and the recurrence is antisymmetric about this time. Note also that the wave form for $t > \tau$ is an inverted (because of the rotated polarization) replica of the fundamental response shown in Fig. 1(a). To model this response with harmonic oscillator equations, it is necessary to first introduce a time delay τ accounting for the recurrence. Second, it is necessary to introduce two harmonic oscillator equations: one accounting for $t > \tau$ and the other for $t < \tau$. A single equation delayed by τ would reproduce the curve shown in Fig. 1(a) but shifted by τ. To capture the response for $t < \tau$, a second equation must be introduced that is integrated backward in time. The two equations are written

$$\left[\frac{d^2}{d\xi^2} \pm 2\gamma_N \frac{d}{d\xi} + \omega_N^2\right] \chi^{ns}_{\mathrm{rot},\pm} = \pm \frac{1}{2\pi}\omega_N^2 \bar{n}_{2,N} I_0 |a_1(\xi - c\tau)|^2, \tag{17}$$

where a_1 is the vector potential for the first laser pulse. The total delayed susceptibility caused by the pump is then $\chi^{ns}_{\mathrm{rot}} = \chi^{ns}_{+} + \chi^{ns}_{-}$, where the superscript ns refers to the susceptibility not generated by the second pulse itself. A comparison, showing reasonable agreement near the recurrence time of Eq. (17) with the full density-matrix results is presented in Fig. 1(b). In Fig. 1(b), the polarization of the probe pulse is rotated 90° with respect to the pump pulse's polarization. The result of the cross polarization is the introduction of an additional factor of $-1/2$ into Eq. (17). The total rotational susceptibility for the first and second pulses is then $\chi_{\mathrm{rot}} = \chi^{s}_{\mathrm{rot}}$ and $\chi_{\mathrm{rot}} = \chi^{s}_{\mathrm{rot}} + \chi^{ns}_{\mathrm{rot}}$, respectively.

B. Ionization and plasma response

During self-focusing, the laser pulse intensity can become large enough to ionize the nitrogen and oxygen, generating free electrons. The free-electron dipole oscillation in the laser field is π out of phase with the bound-electron dipole oscillation. As a result, the free-electron-plasma susceptibility is negative contributing to refraction. The generation of plasma and loss of gas density is governed by the rate equations,

$$\frac{d\rho_e}{d\xi} = \frac{1}{c}[\nu_N\rho_N + \nu_O\rho_O], \tag{18}$$

$$\frac{d\rho_i}{d\xi} = -\frac{1}{c}\nu_i\rho_i, \tag{19}$$

where the ν_i are the intensity-dependent ionization rates. Noting that $\vec{p}_{pl} = -e^2\vec{E}/m\omega^2$, Eq. (18) can be expressed as an equation for the time evolution of the plasma susceptibility,

$$\frac{d\chi_{pl}}{d\xi} = -\frac{1}{c}\frac{e^2}{m\omega^2}[\nu_N\rho_N + \nu_O\rho_O]. \tag{20}$$

The ionization rates are calculated via the Popruzhenko, Mur, Popov, and Bauer (PMPB) model [26], which involves only two parameters: the ionization energy U_I and the post-ionization atomic core charge Z. For low frequencies, the PMPB model limits to the multiphoton ionization rates in which the electron becomes ionized by transitioning through intermediate excited states in discrete steps of the laser pulse photon energy. For N photon absorption, $\nu \propto I^N$, where $N = \langle U_I/\hbar\omega_0 + 1\rangle$ and the brackets indicate rounding down to the nearest integer. For high intensities, the PMPB model limits to the tunneling ionization rates where the electric field of the laser pulse modifies the molecular potential such that previously disallowed unbound states are accessible through tunneling. In the tunneling limit, $\nu \propto \exp[-\beta U_I^{3/2}/I^{1/2}]$. Because the PMPB model is an ionization model for atoms, some of the parameters must be adjusted to recover the ionization rate for molecules. Here, we use the values quoted by Talebpour *et al.* for nitrogen $U_N = 15.6$ eV and $Z = 0.9$, whereas, for oxygen $U_O = 12.1$ eV and $Z = 0.53$ [25]. The ionization rates as a function of intensity are shown in Fig. 2. Around $I = 2\times10^{14}$ W/cm^2, multiphoton ionization transitions into tunneling ionization.

During the process of ionization, energy is transferred from the laser pulse to the electrons. Thus, in addition to the plasma response, there is an imaginary component of the susceptibility representing ionization depletion of the laser pulse. Following Sprangle *et al.* [11], the total energy loss is simply the product of the energy required for ionization and the number of free electrons generated. The energy loss due to ionization along the propagation path is then

$$\frac{d}{dz}U_{ion} = -\int (U_N\rho_{e,N} + U_O\rho_{e,O})d\sigma, \tag{21}$$

where $\rho_{e,j}$ denotes the plasma density created from that particular gas species and σ is the cross-sectional area. Noting that $U_L \simeq \frac{1}{8\pi}\int d\sigma\, d\xi |k_0A|^2$, the effective susceptibility can be expressed as

$$\chi_{ion} = i\frac{2}{\omega_0}\left[\frac{U_N\nu_N\rho_N + U_O\nu_O\rho_O}{|k_0A|^2}\right]. \tag{22}$$

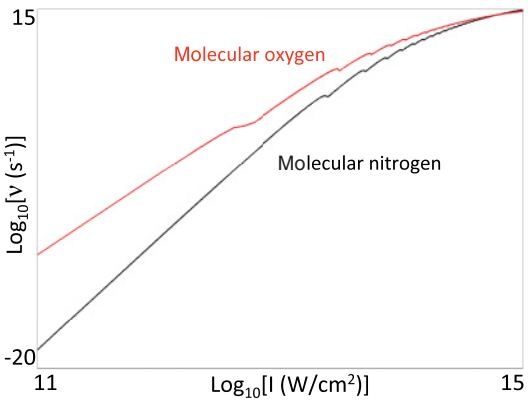

FIG. 2. (Color online) Ionization rates for molecular oxygen and nitrogen as a function of intensity from the PMPB model [26] used in our propagation simulation. For intensities below $I = 1\times10^{14}$ W/cm^2, the generation of plasma is predominately due to the ionization of oxygen molecules.

The total free-electron susceptibility is then $\chi_{free} = \chi_{pl} + \chi_{ion}$.

IV. SIMULATION RESULTS

We solve Eq. (7) numerically in two spatial dimensions, one transverse and one longitudinal, with the susceptibilities defined in Sec. II. We use a split step technique in which we assume the group-velocity dispersion, $\beta_2\partial_\xi^2$, acts independently from diffraction, $\nabla_\perp^2$, for small time steps. The group-velocity dispersion is solved via a dual-sweep matrix inversion. In the second half of the split step, the remaining ξ evolution is treated using a three-point scheme for the derivative [29], whereas, the transverse Laplacian is handled implicitly using a dual-sweep matrix inversion.

Our simulations are based on the experiments reported in Ref. [24]. The propagation of the laser pulse is simulated from a final focusing lens to an aperture, a total propagation distance of 5.5 m. In the experiments, an iris of radius 0.29 cm is placed after the final focusing lens defining the initial radius of the pulse. The initial spatial profile of the pulse is shown in Fig. 3.

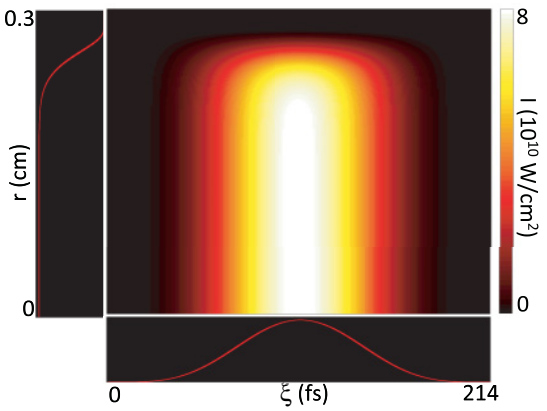

FIG. 3. (Color online) Initial intensity profile of the laser pulse.

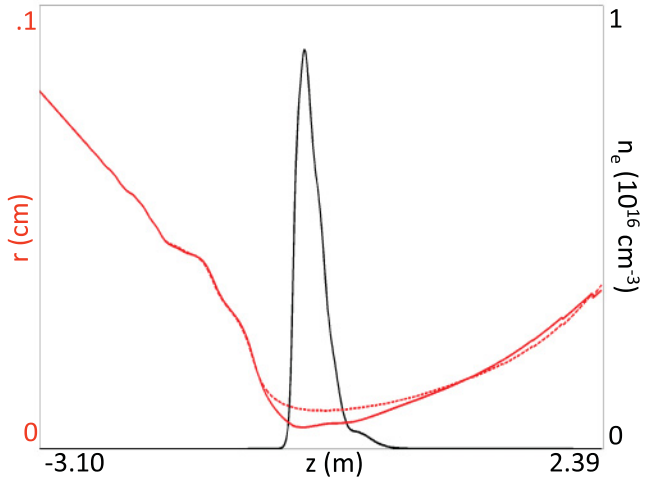

FIG. 4. (Color online) Red line: the radius containing 10% of the pulse power as a function of propagation distance on the left vertical scale. Dotted line: the radius containing 10% for an identical pulse propagating in vacuum is plotted for reference. On the right vertical scale, the electron density is plotted. Self-focusing is evident in the smaller radius of the solid line near the focus. The smaller radius leads to increased intensity and enhanced plasma generation.

The profile is initially flat and transitions to zero at 0.29 cm at the edge of the iris because of numerical issues associated with using an exact flattop profile. The initial transverse phase of the pulse is set as $\phi_t = -\frac{1}{2}k_0 r^2/L_f$, where L_f is the focal length of the lens. The radial extent of the simulation domain is 1.06 times the initial aperture size, and we use 600 radial zones. The initial longitudinal intensity profile is $\sin^4(\pi\xi/\sigma)$ for $0 < \xi < \sigma$ with a corresponding FWHM of $\sigma_{\mathrm{FWHM}} \simeq 0.36\sigma$. The total longitudinal extent of the simulation box is 2σ with 400 zones.

For brevity, we will refer to the first laser pulse as the pump and the second laser pulse as the probe even though the energy of both pulses is comparable. For evaluating the pump's rotational susceptibility experienced by the probe, we record the intensity profile of the pump in both the r and ξ coordinates every 0.8 cm along the entire propagation path. The recorded intensity is then used at the corresponding axial positions when evaluating Eq. (17) for the susceptibility experienced by the probe.

A. Pump propagation

We now consider the individual propagation of the pump with a central wavelength $\lambda = 800$ nm, FWHM $\sigma_{\mathrm{FWHM}} = 77$ fs, and an energy of $U_L = 1.34$ mJ. Figure 4 shows the radius containing 10% of the pulse energy as a function of propagation distance, solid red line, and the electron density created during the filamentation process, sold black line. The 10% radius for the same pulse propagating in vacuum is also plotted as the dashed red line. Self-focusing is evident: near focus, 10% of the laser pulse's power is contained in about half the transverse area as compared to the vacuum propagation case. As the pulse focuses, the intensity becomes large enough to generate a significant electron population, which then causes the pulse power to refract to larger radii.

We define, as follows, "core-average" quantities X, which allows us to better interpret the presences of self-focusing and filamentation that are most active near the axis of propagation,

$$\langle X(a,z)\rangle_{\mathrm{core}} = \frac{2}{R_c^2}\int_0^{R_c} X(a,z,r)d^2r, \tag{23}$$

where $R_c = 200$ μm about 1/15 of the entire radial simulation domain and a is either ξ or its associated Fourier-transform variable. Figure 5(a) depicts the core-averaged laser pulse spectrum as a function of propagation distance. For plotting, the amplitude has been normalized to the maximum at each distance; pump depletion is not observable in the plot. The pulse spectrum remains centered around 800 nm until the pulse begins to focus, at which point, the pulse drives a large molecular alignment, resulting in significant redshifting.

To examine this, we consider the Hamiltonian model for wave-packet dynamics in which the frequency acts as the Hamiltonian, the wave vectors act as the momenta, and the susceptibility acts as the potential. In particular, we can write the Hamiltonian as $(\omega/c) = [(k_z^2 + k_\perp^2)/(1 + 4\pi\chi)]^{1/2}$. Consequently, the evolution of the wavelength shift during propagation can be expressed in terms of the susceptibility as

$$\frac{\partial}{\partial z}\left(\frac{\delta\lambda}{\lambda_0}\right) = 2\pi\frac{\partial\chi_{NL}}{\partial\xi}. \tag{24}$$

In Fig. 5(b), the core average of $\partial_\xi\chi_{NL}$ is plotted as a function of propagation distance and the pulse frame coordinate. The centroid of the pulse is also plotted as the dotted black line. The positive (negative) regions in Fig. 5(b) are where the pulse can acquire red (blue) shifts. The positive region in Fig. 5(b) is the result of the pulse driving a large instantaneous and molecular response in the atmosphere, whereas, the negative region is the decay of the molecular response due to phase mixing, which can be observed in Fig. 1(a).

Ionization also plays a role in $\partial_\xi\chi_{NL}$, but in Fig. 5(b), its susceptibility contribution is not directly noticeable. In Fig. 6, the on-axis total nonlinear susceptibility and the plasma susceptibility are plotted at peak ionization, 50 cm before vacuum focus. The ionization plays a significant role in the total susceptibility but is never large enough to generate a negative gradient in the susceptibility, which, in turn, precludes blueshifting of the laser pulse. Furthermore, we note that the intensity of laser pulse is clamped at an intensity of $\sim 3 \times 10^{13}$ W/cm^2. The plasma response from ionization also reduces the susceptibility reducing the degree of self-focusing.

B. Probe propagation

For the probe pulses, we consider nine delays near one full nitrogen molecule recurrence period each separated by 13 fs. The delays are measured in time with respect to a full recurrence period where the recurrence susceptibility crosses through zero. Figure 7 shows the delays used in the simulation and where their peaks initially lie on the molecular index modification left behind by the pump. The red circles show the probe pulse delays with the polarization rotated 90° from the pump, whereas, the blue triangles are delays for probe pulses with identical polarization as the pump. Most of our investigation will involve probe pulses cross polarized with respect to the pump, which introduces a factor of $-1/2$ in

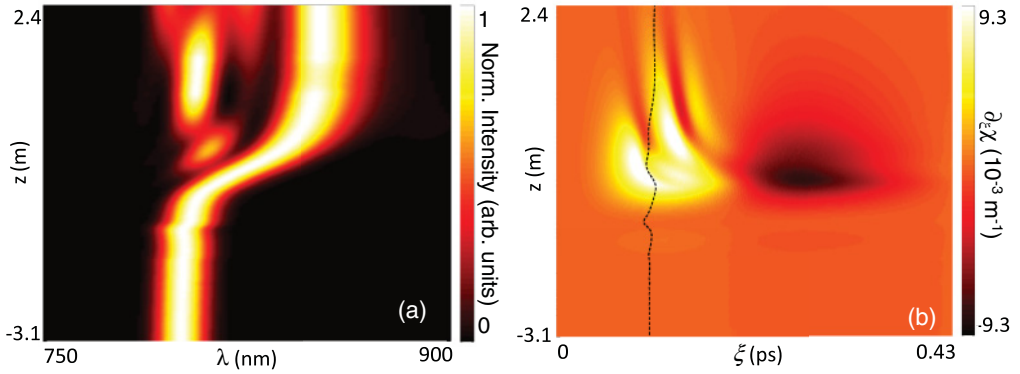

FIG. 5. (Color online) (a) Laser pulse spectrum averaged within the radial core as a function of propagation distance. The intensity has been normalized along the distance. (b) Differential susceptibility averaged within the radial core as a function of propagation distance and position in the moving frame window. The centroid of the laser pulse is plotted as the dashed black line. As the laser pulse self-focuses, the fluence increases, greatly enhancing the molecular wake. The redshifting results from the increase in molecular alignment within the pulse.

the pump's index modification experienced by the probes. However, we briefly consider identical polarization at the end of this section. The recurrence susceptibility acts as a lens that co-propagates with the probe pulses. Unlike a steady lens, however, the index changes along the propagation path due to the evolution of the pump pulse one recurrence period earlier. As with a lens, a larger index of refraction leads to stronger focusing, and we expect probes starting in higher (lower) index phases of the recurrence susceptibility to focus more strongly (weakly). We will refer to the positive and negative regions of recurrence susceptibility as the focusing and defocusing phases, respectively.

In the simulations, the pulse evolution is determined by competition between refraction due to the radial gradient of the index and diffraction. (Phase modulation and dispersion are of secondary importance). Figure 8 depicts the total on-axis electron-density profiles for three probe delays and the initial electron density (black curve) due to ionization by the pump as functions of propagation distance. The density profiles show three types of behavior. For the -52-fs delay, the probe pulse encounters the strongest focusing phase of the pump's recurrence and focuses earlier than the pump. It generates additional plasma, refracts, and still has enough power to focus downstream in the combined pump-probe index, creating the second electron-density population. The -13-fs probe pulse encounters a smaller focusing effect from the pump's recurrence. It focuses slightly earlier than the pump, enhances the existing plasma density but is unable to re-self-focus, and continues to refract without generating an additional plasma population. Finally, the 26-fs probe pulse encounters the defocusing phase of the pump's recurrence, focuses further downstream than the pump, and generates additional plasma closer to the vacuum focus. This behavior is demonstrated more clearly in Fig. 9, which shows the radius containing 10% of the laser power as a function of propagation distance for delays in the middle column of Fig. 8: -52, -13, and 26 fs. The -52-fs delay focuses earliest and refracts the earliest but is able to refocus, the -13-fs delay focuses slightly later, remains collimated and then refracts strongly, while the 26$-$fs delay

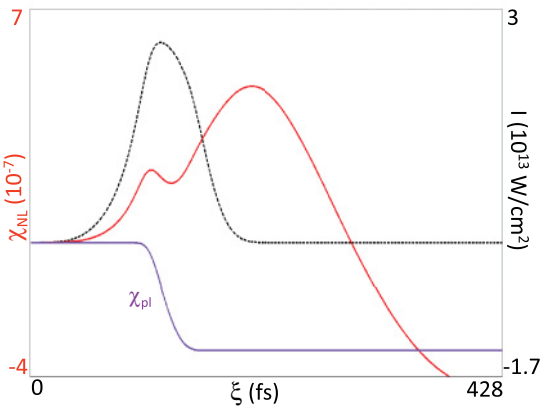

FIG. 6. (Color online) The total on-axis susceptibility at peak ionization, 50 cm before vacuum focus, as a function of the pulse frame coordinate in the solid red curve. The plasma contribution to the total susceptibility is plotted as the purple solid line. The black dotted curve shows the on-axis intensity profile at the same propagation distance. The total susceptibility is positive within the pulse but is significantly reduced by the presence of plasma.

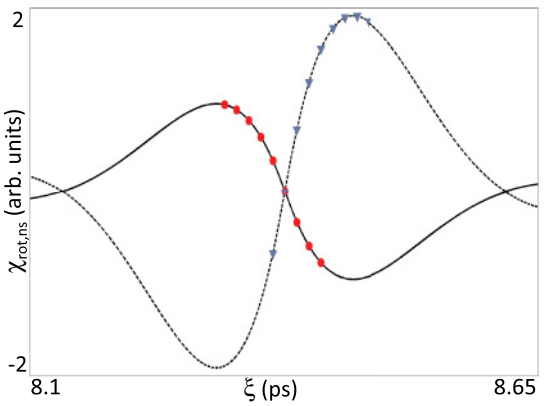

FIG. 7. (Color online) Delays of probe pulses with respect to pump pulse. The red dots show where the peaks of the probe pulses initially fall with respect to the index modification generated by the pump in the cross-polarization simulations. The blue triangles show the delays of the probe pulse in the identical polarization simulations.

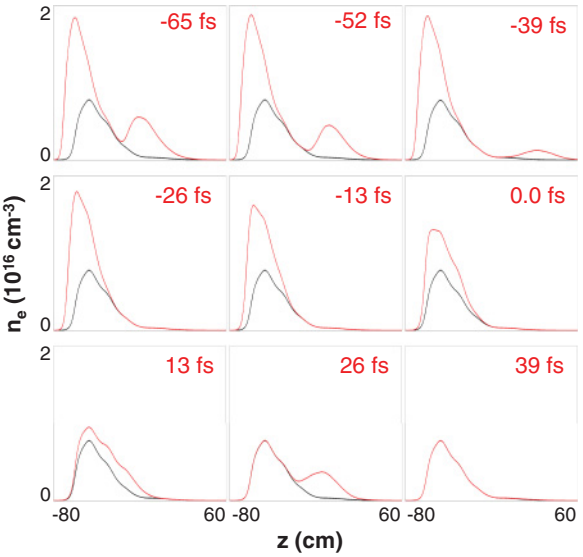

FIG. 8. (Color online) The total electron-density profiles for each probe delay for cross polarization. The red curve is the sum of the electron density initially created by the pump and the additional density generated by the probe. The black curve (at lower densities) shows the initial electron density created by the pump. For the first three delays, the probe pulse experiences the positive index region of the probe's molecular wake and focuses upstream where it generates plasma and refocuses downstream. For the next three delays, the probe starts near the zero crossing of the pump's molecular wake, focuses near the same point, and enhances the existing plasma density. For the last three delays, the probe sees the negative index region, focuses downstream, and generates little to no additional plasma.

focuses the latest and remains collimated over the longest distance.

In Fig. 10, the fraction of power in the core is plotted as a function of propagation distance and pulse frame coordinate for the −52- and 26-fs delays discussed above. The remaining power is contained in the annulus surrounding the core. The white dashed lines demarcate at which propagation distance the electron-density peaks. The fraction of pulse

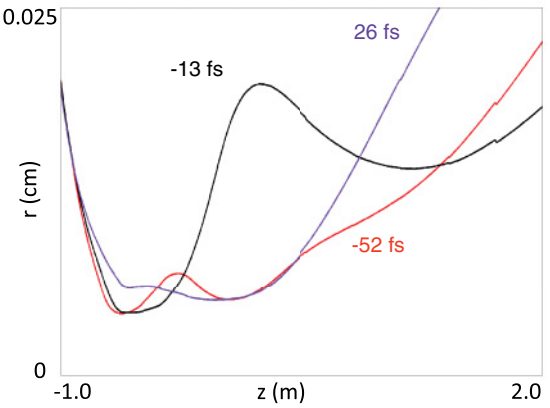

FIG. 9. (Color online) The radius containing 10% of the pulse power as a function of propagation distance for three different probe delays: red curve, −52 fs; black curve, −13 fs; and purple curve, 26 fs. The power remains collimated over the longest distance for the probe delay of 26 fs.

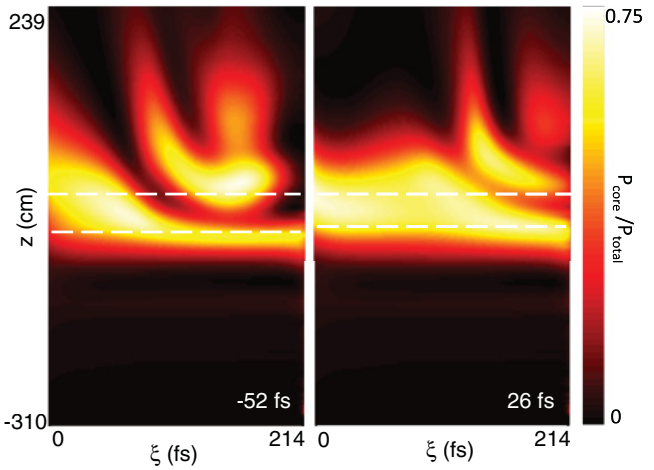

FIG. 10. (Color online) Fraction of power within the core as a function of propagation distance and pulse frame coordinate for two delays: −52 and 26 fs. The dashed white lines show the propagation distances at which the electron density peaks. Each longitudinal position within the pulse focuses and refracts differently. For both delays, the back of the pulse refracts earliest but is able to refocus further downstream.

power within the core provides insight into how the pulse energy is transported transversely at different positions within the pulse. The core intensity acquires a temporal structure due to the different rates of focusing for the different time slices of the pulse. As seen in Fig. 10, there are three distinct transverse dynamics for each region of the pulse. The back of the pulse undergoes three cycles of focusing and refraction, the middle of the pulse undergoes two cycles, and the front of the pulse undergoes one cycle. This is observed as the number of maxima in Fig. 10 as a function of the propagation distance. The refocusing of the back of the pulse is responsible for the creation of the downstream electron density seen in Fig. 8. For the −52-fs delay, the pulse power within the core increases as the pulse focuses. The front of the pulse evolves as if in a weak nonlinear media, focuses near vacuum focus but well after the middle and back of the pulse, then refracts. The back of the pulse focuses slightly before the middle: the rotational susceptibility increases from the front to the back of the pulse. This can be observed as the slanting of the first maxima in the fractional power in Fig. 10. Even before the front of the pulse has focused, the energy in the middle and back of the pulse has diffused transversely. This initial refraction of the middle and back of the pulse is the result of plasma generation.

Figure 11 shows the nonlinear susceptibility experienced at three different time slices, 42, 106, and 171 fs within the −52-fs delay probe pulse as a function of propagation distance and radius. In the front of the pulse, 42 fs, the large susceptibility minimum is due to the electron density generated by the pump pulse. In the middle of the pulse at 106 fs, the hole in the susceptibility is due to a combination of the plasma generated by the pump and the self-generated plasma of the probe. When plasma is generated, its susceptibility contribution is comparable to the molecular and electronic susceptibilities over a small transverse area. This is the result of the ionization rate having a nonlinear relationship to intensity, whereas, the molecular and electron susceptibilities are linear

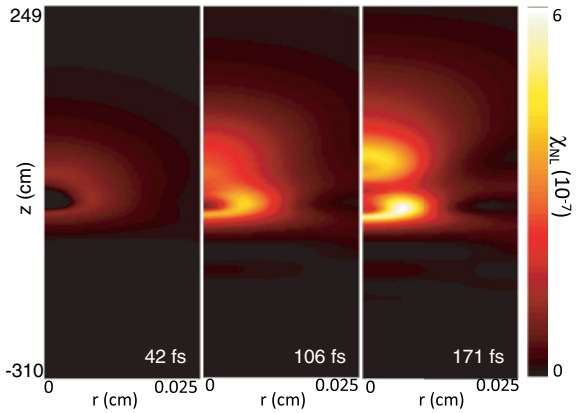

FIG. 11. (Color online) Nonlinear susceptibility as a function of propagation distance and radius for three different positions within the −52-fs delay probe pulse. The transverse dynamics of the front of the pulse (42 fs) are dominated by the molecular wake and plasma density generated by the pump, whereas, the back of the pulse experiences the index modifications of both the pump and itself.

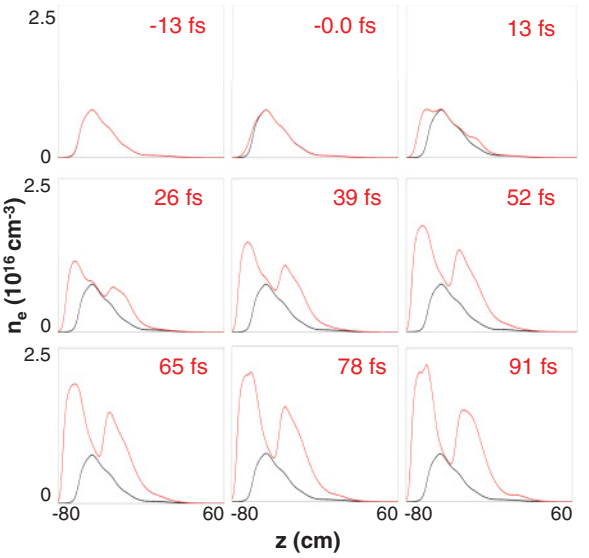

FIG. 12. (Color online) The total electron-density profiles for each probe delay for identical polarization. The red curve is the sum of the electron density initially created by the pump and the additional density generated by the probe. The black curve (at lower densities) shows the initial electron density created by the pump. As the delay time increases, the index experienced by the probe due to the pump's molecular wake increases. The increase in the index of refraction causes the probe to focus more strongly, resulting in additional plasma generation.

in the intensity. The width of the molecular and electronic susceptibilities is approximately the root-mean-squared (RMS) radius of the pulse at peak intensity, whereas, the plasma susceptibility in the N-photon regime is N times smaller than the RMS radius at peak intensity. In the region where plasma is generated, there is a transverse minimum in the susceptibility, which causes the pulse energy to move outward from the center. As the pulse energy is transferred outward, the intensity goes down, and ionization terminates. When ionization terminates, the on-axis minimum vanishes, and the transverse profile of the susceptibility again has a maximum on axis. As seen in the nonlinear susceptibility plot at 171 fs, if the power within the core of the pulse remains sufficiently large after ionization, the pulse can refocus. This process is aided by the recurrence in susceptibility generated by the pump, which reduces the power required for self-focusing. As the pulse refocuses, the intensity goes up, and additional plasma is generated: the second density maxima in the first three profiles of Fig. 8. Again, an ionization index minimum forms, resulting in refraction, and the process can repeat. For the 171-fs slice, there are three index minima. The first is the result of the plasma generated by the probe, the middle is the plasma generated by the pump, and finally, the last minimum is the second density maximum generated by the probe. After refracting from each minimum, the probe pulse refocuses until it finally diffracts away.

For the 26-fs delay, the same features are observable, but they occur farther back in the pulse frame. Here, because the probe pulse initially sits in the defocusing phase of the recurrence, the pulse focuses further downstream and does not focus as strongly. Because the intensity is not as large, less plasma is generated, and the on-axis index minimum is not as severe, causing refraction to occur later. Refraction occurs first in the back of the pulse: an on-axis minimum in the index occurs from the transversely localized plasma contribution of the pump. The region right behind the initial peak of the pulse begins to refract 50 cm further downstream after the creation of the second density population as seen in Fig. 8. However, the front and peak of the pulse, which remain well collimated for close to 1 m after the initial focus, have not refracted yet. As a result, the region right behind the peak experiences a large positive index due to the molecular response as ionization begins to terminate. While the front and peak of the pulse refract away, this region is able to refocus. This leads to the observation of a greatly shortened probe pulse ∼30-fs FWHM within the core after 5.4 m. However, when considering the total power, integrated over all radii, the final FWHM of the probe pulse, ∼75-fs FWHM, is not considerably different from the initial FWHM.

Figure 12 shows the on-axis density profiles resulting from probe pulses with identical polarization to the pump pulse and delays seen as blue triangles in Fig. 7. The general trend is that the enhancement in filament density is larger for pulses starting in the positive rotational susceptibility recurrence: Density increases as initial recurrence susceptibility increases. For delays of 26 fs or longer, two discernible density peaks form separated by 40 cm. The peaks are approximately split by the maximum in pump-generated density. Because the pulses begin in a large positive susceptibility, they self-focus, reach high intensity upstream from the pump pulse, and generate additional plasma earlier. By the same process described above for cross-polarized pulses starting in the positive region of the recurrence susceptibility, the pulses can refocus further downstream and can generate additional plasma.

V. SUMMARY AND CONCLUSIONS

We have considered the propagation through atmosphere 80% N_2 and 20% O_2 of two delayed ultrashort laser pulses either cross or identically polarized. To examine the

propagation, a self-consistent paraxial propagation simulation was developed that includes physics models for the instantaneous electronic response, delayed rotational response, plasma response, and ionization energy damping. For the models of the instantaneous and delayed response, calibrations were performed using recent experimental results [27]. The delayed responses were also calibrated using density-matrix simulations [7].

In addition to the self-index modifications described above, a computationally efficient model for the index due to rotational recurrences in the oxygen and nitrogen was proposed. The model is a modification of the simple-harmonic oscillator (SHO) model already used for the self-rotational susceptibility. The susceptibility at the full recurrence is found by integrating two delayed SHO equations one forward and one backward in time, which, when summed together, provide the response at one full rotational recurrence period. The response is driven by the pump pulse intensity one recurrence period earlier at the same longitudinal position. This model was also calibrated using density-matrix simulations.

The main focus of this paper was to examine the propagation of probe pulses under the influence of not only their own index modifications, but also the molecular recurrence modification and electron-density profiles generated by the pump pulse. The probe pulses were initialized at various positions within the recurrence index structure. For cross polarization, this resulted in three types of behavior depending on whether the probe began in the focusing or defocusing phase of the recurrence susceptibility. If the initial recurrence susceptibility was positive, the probe pulses would focus upstream compared to the pump pulse, extending the plasma filament in the upstream direction. Additionally, these pulses maintained enough power within their radial core that they were able to refocus further downstream and to generate additional plasma. When the initial recurrence susceptibility was small or zero, the probes would focus near the same longitudinal position as the pump and simply would enhance the electron density already generated. Finally, if the initial recurrence susceptibility was negative, the probe pulses would focus downstream. This trend is to be expected as the larger (smaller) the index of refraction, the stronger (weaker) the focusing.

Each section of the probe pulse was found to have distinct focusing dynamics. The front of a probe pulse generated little self-index modification and evolved only due to the plasma density and molecular recurrence modifications generated by the pump. The middle and back of the pulse experienced both self-modifications and the pump's modifications. In particular, it was found that the back of the pulse was responsible for the refocusing downstream and generation of additional electron-density populations. This situation was even more evident when the probe pulse was identically polarized to the pump due to the larger recurrence susceptibility, providing even larger densities in the plasma filament.

ACKNOWLEDGMENTS

The authors would like to thank P. Sprangle, J. K. Wahlstrand, A. Fallahkhair, W. Zhu, L. Johnson, T. Rensink, and N. Jain for fruitful discussions. The authors would also like to thank the ONR, NSF, and DOE for support.

APPENDIX: ENERGY AND ACTION

In this appendix, we consider how the source term $4\pi\,\partial_\xi P_{NL}$ in the wave equation, representing frequency shifts of the polarization, affects the energy evolution of the laser pulse. For simplicity, we ignore dispersion $\beta_2 \simeq 0$ and approximate $c_f \simeq c$. Equation (7) with the additional term is then

$$\left[2\frac{\partial}{\partial z}\left(ik_0 - \frac{\partial}{\partial\xi}\right) + \nabla_\perp^2\right]A = 4\pi\left(ik_0 - \frac{\partial}{\partial\xi}\right)\chi_{NL}\left(ik_0 - \frac{\partial}{\partial\xi}\right)A, \tag{A1}$$

where we have written $P_{NL} = -\chi_{NL}(ik_0 - \partial_\xi)A$. Upon multiplying Eq. (A1) by $-(ik_0 + \partial_\xi)A^*$ and adding the complex conjugate, we have

$$\frac{\partial}{\partial z}\int\left|\left(ik_0 - \frac{\partial}{\partial\xi}\right)A\right|^2 d\vec{x} = -4\pi\int\left|\left(ik_0 - \frac{\partial}{\partial\xi}\right)A\right|^2\frac{\partial\chi_{NL}}{\partial\xi}d\vec{x}, \tag{A2}$$

where we have taken χ_{NL} to be real. Identifying the LHS with the laser pulse energy and using $U_L \simeq \frac{1}{8\pi}\int d\sigma\, d\xi|(ik_0 - \partial_\xi)A|^2$, we can write Eq. (A2) as follows:

$$\frac{\partial U_L}{\partial z} = -\frac{1}{2}\int\left|\left(ik_0 - \frac{\partial}{\partial\xi}\right)A\right|^2\frac{\partial\chi_{NL}}{\partial\xi}d\vec{x}. \tag{A3}$$

Similarly, we can show that the wave action is conserved by multiplying Eq. (A1) by A^* and subtracting the complex conjugate. In particular, $\partial_z I = 0$ where

$$I = \frac{1}{16\pi}\int\left[A^*\left(k_0 + i\frac{\partial}{\partial\xi}\right)A + A\left(k_0 - i\frac{\partial}{\partial\xi}\right)A^*\right]d\vec{x}. \tag{A4}$$

Using the Hamiltonian model for wave-packet dynamics where $H = (\omega/c) = [(k_z^2 + k_\perp^2)/(1 + 4\pi\chi)]^{1/2}$, we can write the longitudinal wave number as

$$k_z = k_0 - 2\pi\int\frac{\partial\chi_{NL}}{\partial\xi}dz. \tag{A5}$$

We identify $\delta k = k_z - k_0$ as the wave-number shift with $\delta k \simeq iA^{-1}\partial_\xi A = -2\pi\int\partial_\xi\chi_{NL}dz$. Substituting $i\,\partial_\xi = \delta k$ into Eqs. (A1) and (A3), we see that these terms provide corrections on the order of χ_{NL}^2 to the phase and energy, respectively. Thus, neglecting the wave-number shifts in the polarization is fine so long as the index contribution due to the nonlinear susceptibility remains small.

[1] A. Couairon and A. Mysyrowicz, Phys. Rep. **441**, 47 (2007).
[2] J. H. Marburger, Prog. Quantum Electron. **4**, 35 (1975).
[3] M. Mlejnek, M. Kolesik, J. V. Moloney, and E. M. Wright, Phys. Rev. Lett. **83**, 2938 (1999).
[4] C. H. Lin, J. P. Heritage, T. K. Gustafson, R. Y. Chiao, and J. P. McTague, Phys. Rev. A **13**, 813 (1976).
[5] J. P. Palastro, T. M. Antonsen Jr., and A. Pearson, Phys. Rev. A **84**, 013829 (2011).
[6] Y.-H. Chen *et al*., Opt. Express **15**, 11341 (2007).
[7] A. J. Pearson and T. M. Antonsen, Phys. Rev. A **80**, 053411 (2009).
[8] H. Stapelfeldt and T. Seideman, Rev. Mod. Phys. **75**, 543 (2003).
[9] E. Hamilton, T. Seideman, T. Ejdrup, M. D. Poulsen, C. Z. Bisgaard, S. S. Viftrup, and H. Stapelfeldt, Phys. Rev. A **72**, 043402 (2005).
[10] A. Braun *et al*., Opt. Lett. **20**, 73 (1995).
[11] P. Sprangle, J. R. Peñano, and B. Hafizi, Phys. Rev. E **66**, 046418 (2002).
[12] J. R. Peñano, P. Sprangle, P. Serafim, B. Hafizi, and A. Ting, Phys. Rev. E **68**, 056502 (2003).
[13] G. Méchain *et al*., Appl. Phys. B: Lasers Opt. **79**, 379 (2004).
[14] G. Méchain, A. Couairon, M. Franco, B. Prade, and A. Mysyrowicz, Phys. Rev. Lett. **93**, 035003 (2004).
[15] A. Ting *et al*., Appl. Opt. **44**, 1474 (2005).
[16] S. Eisenmann, J. Peñano, P. Sprangle, and A. Zigler, Phys. Rev. Lett. **100**, 155003 (2008).
[17] Y.-H. Chen, S. Varma, T. M. Antonsen, and H. M. Milchberg, Phys. Rev. Lett. **105**, 215005 (2010).
[18] R. A. Bartels, T. C. Weinacht, N. Wagner, M. Baertschy, C. H. Greene, M. M. Murnane, and H. C. Kapteyn, Phys. Rev. Lett. **88**, 013903 (2002).
[19] G. Fibich *et al*., Opt. Express **13**, 5897 (2005).
[20] A. York and H. M. Milchberg, Opt. Express **16**, 10557 (2008).
[21] S. Varma, Y.-H. Chen, and H. M. Milchberg, Phys. Rev. Lett. **101**, 205001 (2008).
[22] S. Zhdanovich, A. A. Milner, C. Bloomquist, J. Floß, I. S. Averbukh, J. W. Hepburn, and V. Milner, Phys. Rev. Lett. **107**, 243004 (2011).
[23] S. Varma *et al*. (unpublished).
[24] F. Calegari, C. Vozzi, and S. Stagira, Phys. Rev. A **79**, 023827 (2009).
[25] A. Talebpour *et al*., Opt. Commun. **163**, 29 (1999).
[26] S. V. Popruzhenko, V. D. Mur, V. S. Popov, and D. Bauer, Phys. Rev. Lett. **101**, 193003 (2008).
[27] J. K. Wahlstrand, Y.-H. Cheng, and H. M. Milchberg, Phys. Rev. A **85**, 043820 (2012).
[28] E. R. Peck and K. Reeder, J. Opt. Soc. Am. **62**, 958 (1972).
[29] W. Zhu *et al*., Phys. Plasmas **19**, 033105 (2012).